ORIGINAL RESEARCH ARTICLE

Enhancement of Hole Extraction in Carbon-Based Organic–Inorganic Hybrid Perovskite Solar Cells Using MAPbI$_3$:NiO-NPs Composite

R. Isaac Daniel[1] · R. Govindaraj[1] · P. Ramasamy[1] · A. K. Chauhan[2,3,4]

Abstract

In this article, a combination of spherical and oval NiO nanoparticles were synthesized through the co-precipitation method and incorporated into a MAPbI$_3$-based perovskite layer (MAPbI$_3$:NiO) to enhance hole extraction in carbon-based perovskite solar cells (CPSCs). Field-emission scanning electron microscopy (FESEM) images of the MAPbI$_3$ and MAPbI$_3$:NiO NPs composite layers confirmed the formation of needle-like grains. The incorporation of NiO NPs in the perovskite layer enhanced both the crystallinity and the grain size of the film. Moreover, the NiO composited films showed maximum absorbance in the visible region and significantly quenched emission peak in the photoluminescence (PL) emission spectrum. Because of the materials' outstanding characteristics, the NiO composite perovskite device achieved power conversion efficiency (PCE) of 9.75%. In addition, the effect of adding a spacer layer in the same device architecture was also studied. The results showed an enhancement of the open-circuit voltage (V_{oc}) from 862 mV to 988 mV, making the device a champion with PCE of ~11%.

Graphical Abstract
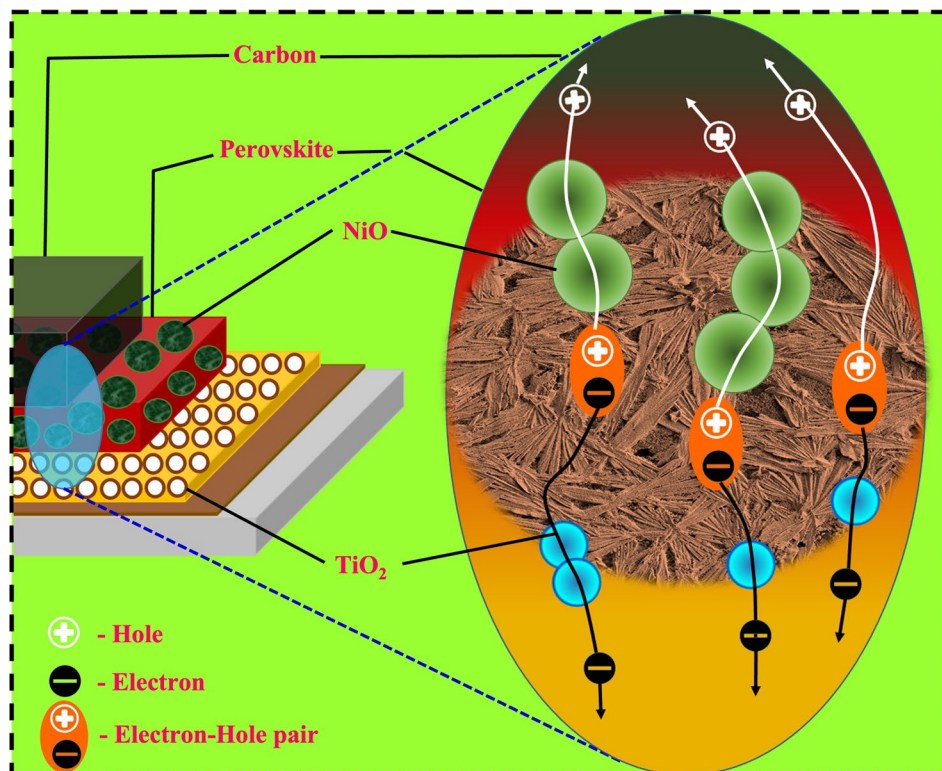
Extended author information available on the last page of the article

Introduction

Over the past decade, perovskite solar cells (PSCs) have gained prominence as the leading technology in next-generation solar cells. They are based on organic and inorganic lead halide perovskites. The general formula for perovskite is ABX$_3$, in which A, B, and X are monovalent cation, divalent metal cation, and halogen, respectively. The superior properties of MAPbI$_3$ perovskite including high carrier mobility, low exciton binding energy (40 meV), large carrier diffusion length (>1000 nm), and high absorption coefficient (10^5 cm^{-1}) along with advantages of simple solution processing and low cost have made them a focus of research in the field of PSCs.[1–5]

The conventional n-i-p architecture of PSCs consists of the following layers. (i) The transparent conducting oxide (TCO) helps to conduct electrons to the external load. (ii) The electron transport layer (ETL) simultaneously acts as a scaffold for the growth of perovskite and transports electrons from the perovskite absorber. TiO$_2$,[5] SnO$_2$[6] and ZnO[7] are the most commonly employed electron transport materials (ETM). (iii) The perovskite absorber is also known as the heart of the PSC. MAPbI$_3$[8] and FAPbI$_3$[9] are commonly used as perovskite absorbers. (iv) The hole transport layer (HTL) aids in the extraction of holes from the perovskite absorber to reduce electron–hole recombination. Spiro-OMeTAD[10] and poly(3-hexylthiophene-2,5-diyl) (P3HT)[11] are the most commonly used hole transport materials (HTM). (v) Noble metal electrodes serve as the top electrodes. Gold (Au) and silver (Ag) are commonly used for such metal contacts. The cost of both noble metals and organic HTMs (spiro-OMeTAD and P3HT) is very high, and at the same time they require high vacuum technology for the deposition of metal electrodes. These factors will constitute a bottleneck for the commercialization of the PSC in the future, and therefore, several studies are ongoing worldwide to reduce the cost of PSCs.

To find an alternative for the high-cost noble metal electrodes, Hand et al. first utilized a low-cost carbon electrode in the PSC instead of a metal electrode and succeeded in obtaining PCE of 6.6%.[12] The carbon-based PSCs utilize commercial industrial technology to permit carbon electrodes to reduce the influence of moisture on the perovskite layer, thus increasing the device stability. It also demonstrates good compatibility with screen printing, blade coating, and other printing methods. Consequently,

carbon-based PSCs have become an important candidate for the commercialization of PSCs.[13]

On the other hand, an alternative low-cost HTM is needed for spiro-OMeTAD because, in addition to its high cost, its instability factor also constrains commercialization. In contrast to the expensive and chemically degradable organic hole-transport materials (HTMs), inorganic HTMs have gained significant recognition due to their low-cost synthesis, well-matched energy level to perovskites, efficient hole transfer caused by their relatively high conductivity, and chemical inertness. Thus, the substitution of the organic HTM for the inorganic one helps to reduce the cost of materials and improve device stability. In recent years, inorganic HTMs such as CuSCN,[14,15] CuI,[16] and NiOx[17–20] have been used as HTM for PSCs, and the corresponding devices achieve high PCE. Among them, NiO is established as a successful HTM because of its high hole mobility, chemical stability, hydrophobic nature, and ability to act as an electron blocking layer.[21] It has a wide band gap (Eg) and deep valence band (VB) that aligns well with the highest occupied molecular orbital (HOMO) levels of many p-type organic semiconductors.[22] Because of these superior properties, NiO is utilized as an HTM in organic light-emitting diodes (OLED) and organic optoelectronic devices such as organic photovoltaic (OPV) cells.[23] As mentioned above, NiO has been successfully utilized as an HTM in perovskite-based PV technology. The majority of high-performance p-i-n type perovskite PV devices with NiO as the HTL have been fabricated using high-cost techniques such as pulsed-laser deposition (PLD) and sputtering.[24] Park et al. fabricated perovskite PV devices on nanostructured NiO prepared by PLD that demonstrated average PCE of 15.3% (maximum 17.3%).[25] Fang et al. used NiO$_x$ film in perovskite PV cells prepared by sputtering and reported maximum PCE of 18.7%.[26] Therefore, a simple and low-cost method is needed to utilize NiO as HTM in PSCs for its commercialization.

In work article, we synthesized p-type NiO semiconductor material with the capping agent ethylenediaminetetraacetic acid (EDTA) through the co-precipitation method, and it was incorporated into the perovskite layer. It was observed that incorporating a small amount of NiO into the perovskite precursor could achieve enhanced crystallinity with needle-like grains and reduced non-radiative recombination. The optical properties of the perovskite films with different weight percentages of NiO were examined by UV-Vis and photoluminescence (PL) emission spectroscopy. The effect of the incorporation of NiO NPs on the perovskite

grain growth was studied using field-emission scanning electron microscopy (FESEM) images. The $MAPbI_3$:NiO NP composition had a strong impact on photocurrent density and charge extraction, which was investigated by fabricating a simple and low-cost carbon-based perovskite solar cell. An additional layer in the same CPSC, called the spacer layer, which was based on the same NiO, was applied before the perovskite layer, and its advantage in improving the open-circuit voltage and charge extraction was investigated. The glass/fluorine-doped tin oxide (FTO)/c-TiO$_2$/mp-TiO$_2$/MAPbI$_3$:NiO/carbon device achieved PCE of 9.75%, with J_{sc} of 21.67 mA/cm^2, V_{oc} of 862 mV, and a fill factor of 52.2%. On the other hand, the device having a spacer layer with architecture of glass/FTO/c-TiO$_2$/mp-TiO$_2$/NiO/MAPbI$_3$:NiO/carbon achieved PCE of ~11%, with J_{sc} of 22.11 mA/cm^2, V_{oc} of 988 mV, and a fill factor of 50.2%. Moreover, $MAPbI_3$:NiO-based single-junction CPSCs exhibited an extraordinary improvement in current density when compared to devices with pristine perovskite ($MAPbI_3$) layers.

Experimental

Materials

Nickel chloride hexahydrate ($NiCl_2.6H_2O$), sodium hydroxide (NaOH), N,N-dimethylformamide (DMF), hydrochloric acid (HCl), and butanol were purchased from Merck. Lead iodide (PbI_2) and dimethyl sulfoxide (DMSO) were supplied by TCI. Methylammonium iodide (MAI), Ti-nanoxide, Ni-nanoxide, and FTO substrates were purchased from Solaronix (Switzerland). Titanium diisopropoxide bis(acetylacetonate) was purchased from Sigma-Aldrich. Ethylenediaminetetraacetic acid ($C_{10}H_{16}N_2O_8$) was purchased from SRL. Low-temperature carbon paste was purchased from Dyenamo. Titanium tetrachloride was purchased from Spectrochem. Zinc powder was purchased from Alfa Aesar. All chemicals were used directly without further purification.

Preparation of NiO Powder

NiO powder was synthesized using the co-precipitation method. First, 1 M NiCl$_2$·6H$_2$O was prepared in 100 mL of deionized water, ethylenediaminetetraacetic acid (0.1 M) was added to the above solution as a capping agent, and the mixture was stirred at room temperature. The 4 M NaOH solution was added dropwise to the nickel precursor solution until reaching a pH value of about 10 pH, and the solution was stirred for 1 h at room temperature. The green precipitates were thoroughly washed with deionized water and ethanol. The precipitates were dried at 100°C in a hot air oven

for 12 h. Finally, the green powder was annealed at 500°C for 5 h to yield black NiO powder.

Preparation of Pristine MAPbI$_3$ and NiO-MAPbI$_3$ Composite Solutions

(a) Preparation of pristine MAPbI$_3$ solution:

MAPbI$_3$ solution was prepared by dissolving 1 M each of PbI$_2$ and MAI in 1 mL of a mixed solution of DMF and DMSO (volume ratio 3:1).

(b) Preparation of NiO-MAPbI$_3$ composite solution:

The NiO-perovskite composite solution was prepared from PbI$_2$ (1 M) and MAI (1 M) with 10 mg, 20 mg, 30 mg, and 40 mg of prepared NiO NP powder separately in 1 ml of a mixed solvent of DMF and DMSO (volume ratio 3:1).

The obtained solutions were dispersed using a bath sonicator and then stirred for 12 h at 70°C. The pristine MAPbI$_3$ and NiO-MAPbI$_3$ composite solutions (10, 20, 30, and 40 mg/mL^{-1}) were designated as MAPbI$_3$, N-10, N-20, N-30, and N-40, respectively.

Device Fabrication

The entire process of fabrication was done under ambient conditions except the deposition of the perovskite layer, which was done under an argon atmosphere. The FTO substrates were patterned by Zn powder and HCl. The patterned FTO substrates were sequentially sonicated with deionized water and ethanol for 15 min. Then the substrates were cleaned in a UV-ozone cleaner for 15 min to avoid unwanted organic moieties. The compact TiO$_2$ layer solution was spin-coated on the cleaned FTO substrates at 4000 rpm for 30 s using 0.2 M titanium diisopropoxide bis(acetylacetonate) in butanol and annealed at 500°C for 30 min. Subsequently, mesoporous TiO$_2$ solution was prepared by diluting TiO$_2$ paste with absolute ethanol at a 2:7 weight ratio. The prepared solution was spin-coated on the c-TiO$_2$ layer at 4000 rpm for 30 s and sintered at 500°C for 30 min. TiCl$_4$ treatment of the m-TiO$_2$ layer was performed by immersing the m-TiO$_2$ films in a TiCl$_4$ solution at 70°C for 30 min. Then, the film was washed with ethanol and sintered at 500°C for 30 min. For NiO spacer layer devices, the NiO layer was prepared over the m-TiO$_2$ layer by spin-coating a colloidal solution which was prepared by diluting Ni-nanoxide paste with ethanol at a 1:5 weight ratio. The prepared NiO solution was spin-coated on the m-TiO$_2$ at 4000 rpm for 30 s followed by sintering at 500°C for 30 min. Both the m-TiO$_2$- and NiO/m-TiO$_2$-based substrates were taken into the Ar-filled glove box and pre-heated at 100°C for 10 min. The perovskite layer was deposited on the pre-heated substrates by dropping the prepared perovskite solution and spun by a two-step spin-coating method at 1000 rpm for 10 s and 5000 rpm for 30 s. The resultant film was immediately

annealed at 110°C for 15 min. Finally, the carbon paste was deposited by blade-coating on the perovskite layer and dried at 120°C for 15 min. The active area of CPSC was 0.25 cm^2.

Characterization

The structural properties of the synthesized NiO particles and perovskite thin films were validated using a PANalytical Empyrean x-ray diffractometer equipped with a CuKα (CuKα1 = 1.540598 Å) radiation source. The structural morphology of the perovskite films was investigated by FESEM (Carl Zeiss Neon 40 instrument). Elemental analysis was done using energy-dispersive x-ray spectroscopy (EDS). The UV–visible absorption spectra were recorded using a Shimadzu UV 2600i UV-Vis spectrophotometer. The PL measurements were recorded using a Hitachi F-7000 fluorescence spectrophotometer. The thermal stability of carbon was measured by a PerkinElmer Diamond thermogravimetric analyzer (TGA). The current density–voltage (J–V) curves were studied using a Keithley 2400 source meter under a Sciencetech solar simulator (class AAA) under AM 1.5G with one sun illumination of 100 mW/cm^2. External

quantum efficiency (EQE) was studied for the fabricated solar cells using a QE-R instrument from Enlitech, Taiwan.

Results and Discussion

XRD of NiO NPs

Figure 1 shows the powder x-ray diffraction (PXRD) pattern of the synthesized NiO nanoparticles. The diffraction peaks at 2θ are 37.14°, 43.11°, 62.74°, 75.29°, and 79.18°, which correspond to (111), (200), (220), (311), and (222), respectively. These peaks are perfectly matched to the face-centered cubic (FCC) crystalline structure of NiO, which is consistent with the standard spectrum (JCPDS card number 47-1049).[27] The sharp and intense peak reveals the high crystallinity of the synthesized sample. The absence of peaks related to EDTA and elemental Ni confirms that the synthesized NiO powder is highly pure with no impurities. The average crystallite size of the NiO NPs was calculated using the Scherrer formula, as follows.[27]
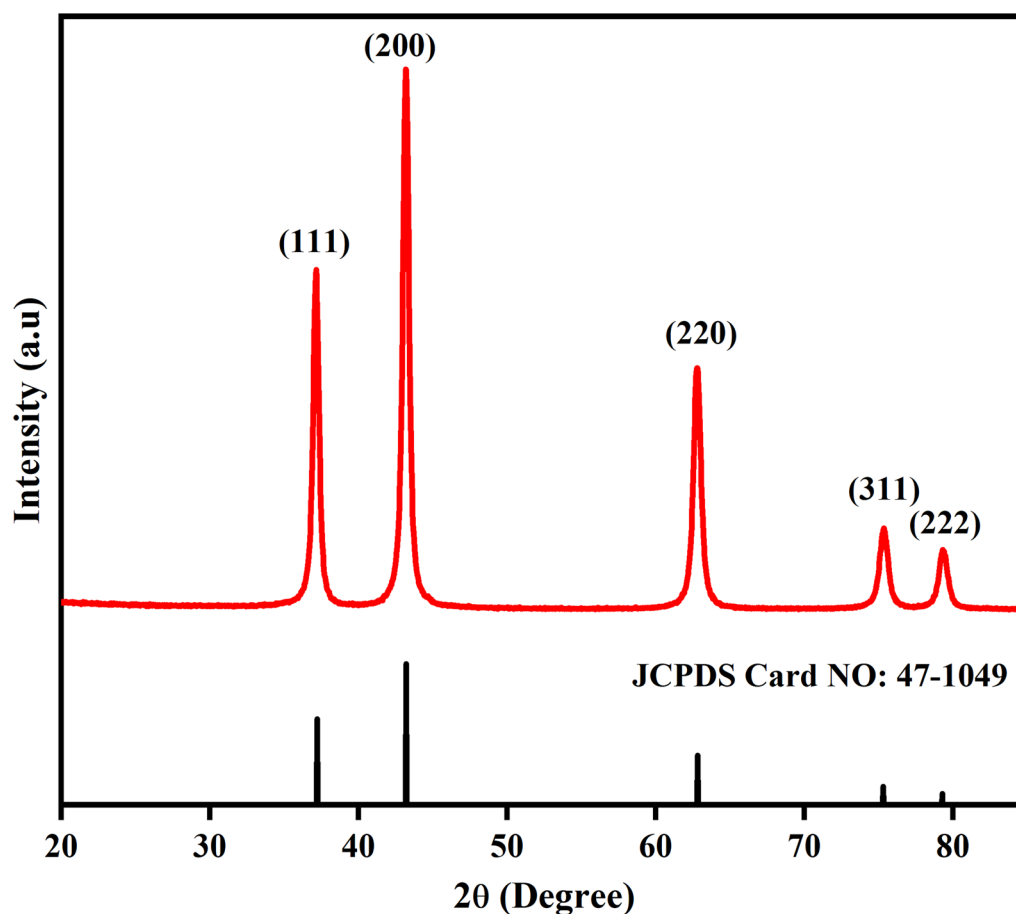

Fig. 1 Powder x-ray diffraction pattern of NiO NPs.

$$D = \frac{k\lambda}{\beta\cos\theta} \qquad (1)$$

where $\lambda = 1.540598$ Å is the wavelength of the x-ray, β is the FWHM (full width at half maximum), θ is the diffraction angle obtained from 2θ values, and k is an empirical constant. The calculated average crystallite size of the NiO nanoparticles was 23.4 nm, as determined by the (111) plane.

UV-Visible-NIR Analysis of NiO NPs

A Tauc plot was used to find the optical band gap edge (E_g) of the synthesized NiO NPs. The energy-dependent absorption coefficient can be expressed by the following equation.[28]

$$(\alpha h\upsilon)^{1/n} = A(h\upsilon - Eg) \qquad (2)$$

where α is the absorbance coefficient, h is the Planck constant, A is the proportionality constant, and υ is the photon frequency. For a direct band transition, the exponent value (n) is 1/2. The Tauc plot of the NiO NPs is shown in Fig. 2.

The band gap of 3.30 eV was identified for synthesized NiO NPs by extrapolating the linear part of the plot to the x-axis.

FESEM Image of NiO NPs

Figure 3a shows the FESEM image of NiO nanoparticles synthesized via the co-precipitation method, which reveals the details of size and morphology. It is evident that the prepared NiO nanoparticles have a mixture of spherical and oval shapes. The average particle size of the synthesized sample was calculated by measuring the size of 70 particles randomly across the reported image using ImageJ software. Figure 3b shows the particle size distribution histogram of NiO nanoparticles which was obtained from the software. It is clear that the particle sizes have a small and narrow size distribution ranging from 15 nm to 40 nm, and the average diameter is about 25 nm.

XRD of MAPbI₃ and MAPbI₃:NiO Thin Films

Figure 4 shows the XRD pattern of the MAPbI$_3$ film without and with NiO NP composite (N-10, N-20, N-30, and N-40). The strong diffraction peaks at 14.07° and 28.40° of 2θ in the XRD pattern correspond to the (110) and (220)
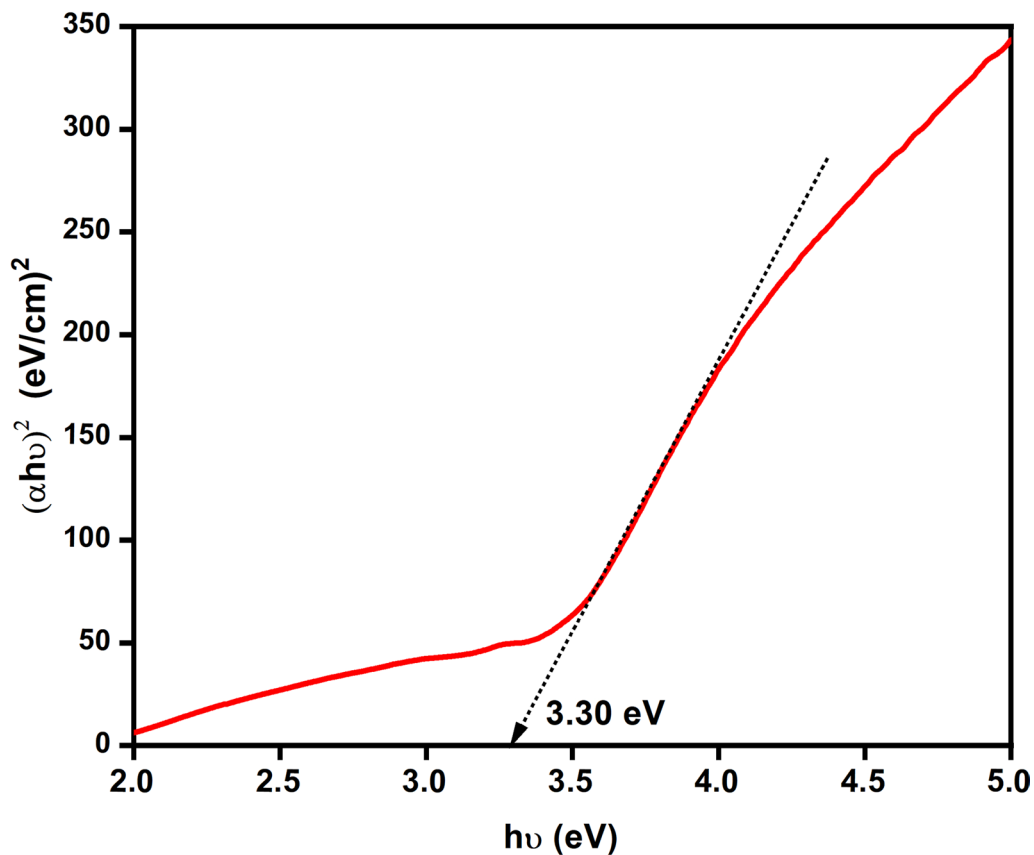
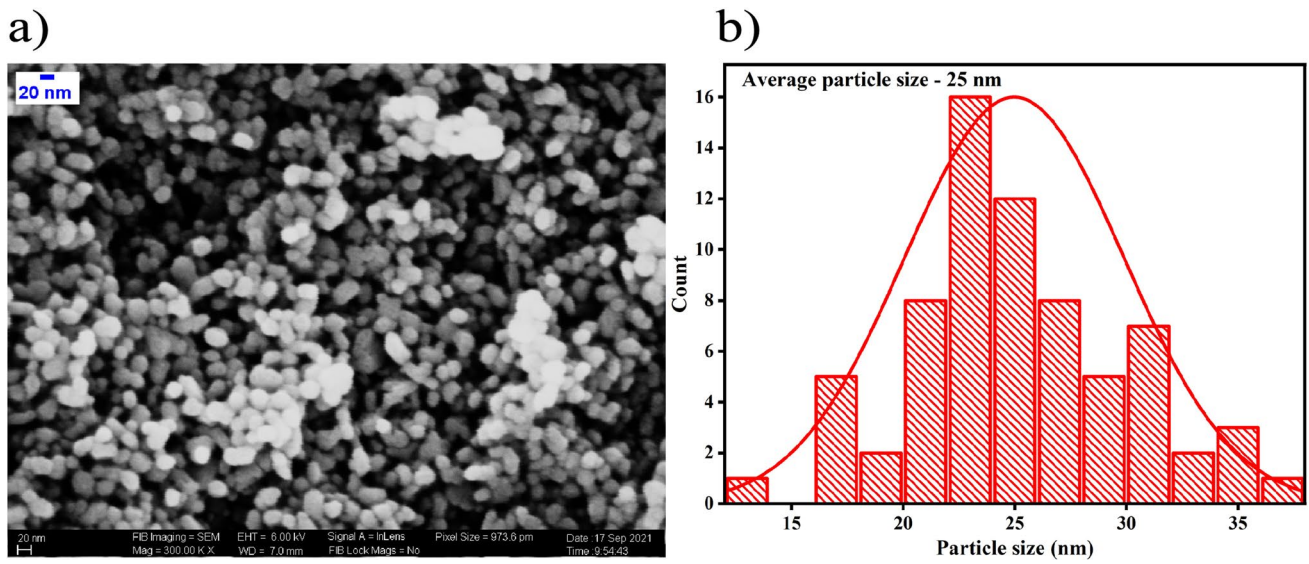**Fig. 2** Tauc plot of the synthesized NiO NPs.

a)

b)

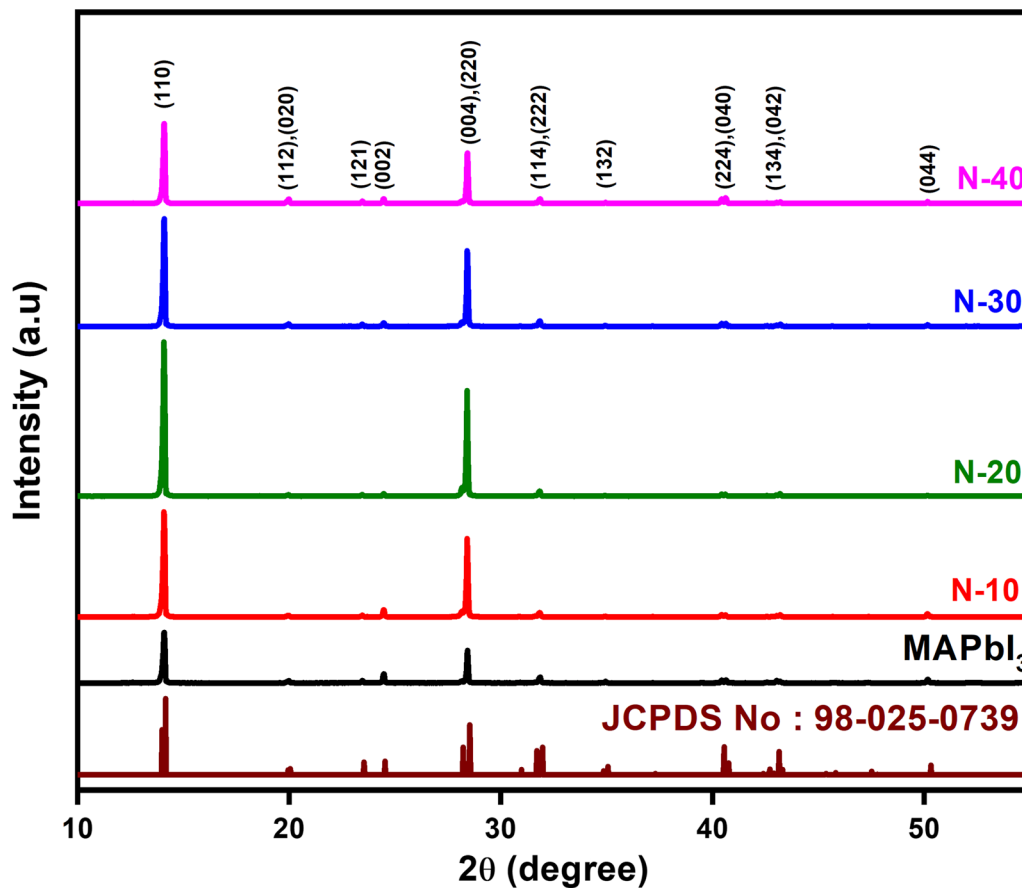Fig. 3 (a) FESEM image and (b) diameter distribution histogram of NiO NPs.

Fig. 4 XRD pattern of pristine MAPbI$_3$, N-10, N-20, N-30, and N-40 films.

diffraction planes of MAPbI$_3$, and the smaller diffraction peaks at 19.89°, 19.94°, 23.45°, 24.45°, 28.13°, 31.59°, 31.85°, 34.93°, 40.42°, 40.62°, 42.56°, 43.02°, 43.17°, 45.68°, 47.36°, and 50.16° of 2θ correspond to (112), (020), (121), (002), (004), (114), (222), (132), (224), (040), (141), (134), (042), (332), (143), and (044) crystal planes of the conventional MAPbI$_3$ tetragonal structure, respectively. No additional peaks related to PbI$_2$ and MAI were observed in the XRD pattern.[29] The major peak intensities of the respective films increased as the concentration of NiO NPs in the perovskite precursor solution was increased up to 20 mg mL^{-1}. The diffraction peak's intensity of the films N-30 and N-40 was suppressed upon further addition of NiO NPs, but not as much as the intensity of the pristine film.

All the perovskite films which contain NiO NPs have a greater diffraction intensity and a smaller FWHM due to their higher crystallinity and larger crystallite size, respectively. The crystallite size of the perovskite films was estimated from the diffracted planes by using the Scherrer formula. The estimated crystallite sizes of MAPbI$_3$, N-10, N-20, N-30, and N-40 were 76.11 nm, 82.02 nm, 86.77 nm, 83.81 nm, and 83.01 nm, respectively.

The obtained FWHM value and estimated crystallite sizes of the perovskite films are shown in Fig. 5a. It is observed that all the NiO NP-composite perovskite films have lower FWHM values when compared to pristine perovskite film. These NiO nanoparticles may induce microstrain in the perovskite films which could be generated from dislocations, crystal imperfections, and defects (vacancy defects, interstitial defects).[30] The following equation (Williamson-Hall) was used to estimate the microstrain (ε):

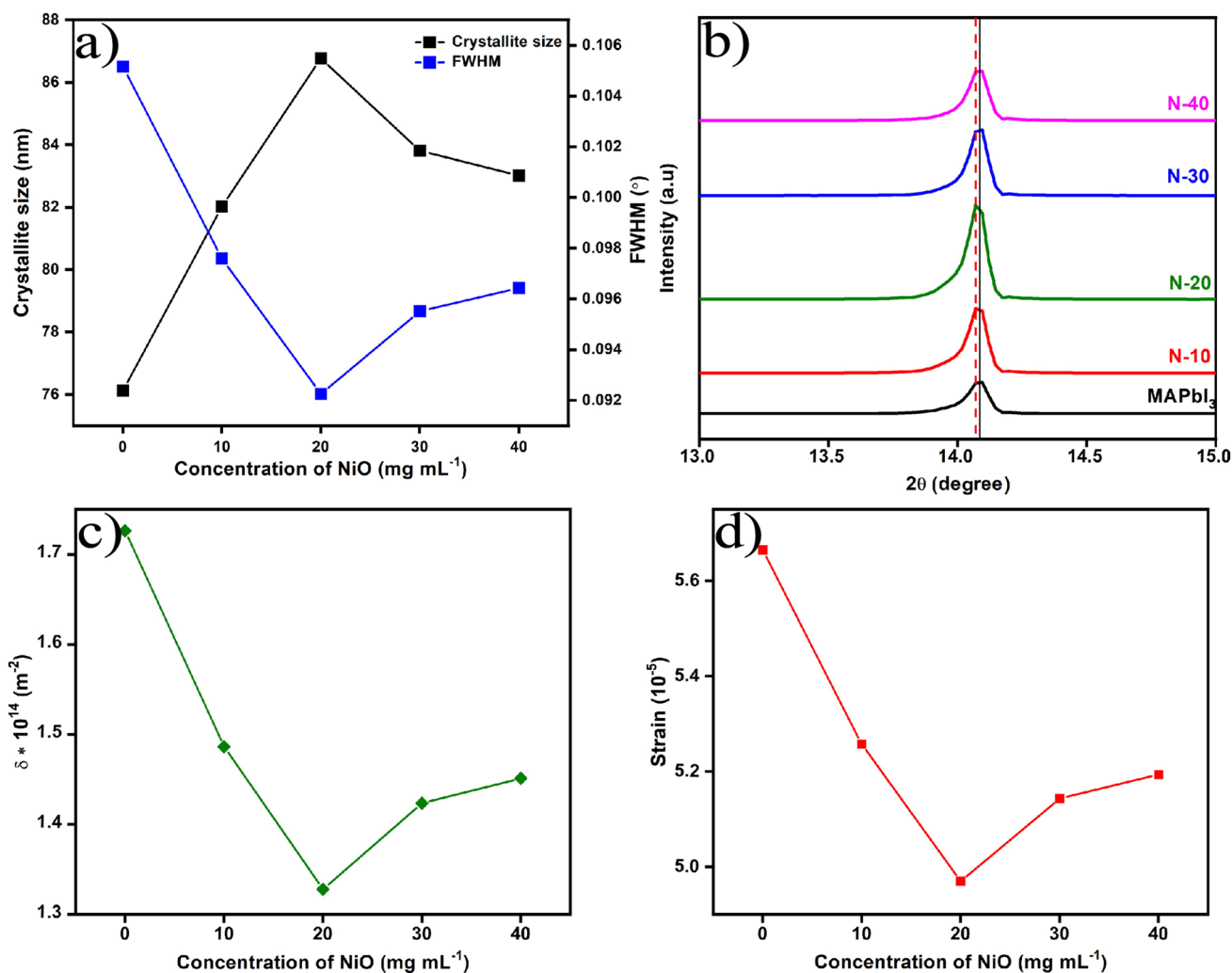$$\beta \cos \theta = 4\varepsilon \sin \theta + K\lambda/D. \tag{3}$$

Fig. 5 (a) Graph of FWHM vs. crystallite size vs. concentration of NiO. (b) Enlarged XRD pattern from 13° to 15°. (c) Dislocation density and (d) strain of pristine MAPbI$_3$, N-10, N-20, N-30, and N-40.

$$\varepsilon = \frac{\beta}{4\tan\theta} \quad (4)$$

The dislocation density (δ) was calculated from the crystallite size (D) using the following expression:

$$\text{Dislocation density, } \delta = \frac{n}{D^2} \quad (5)$$

where *n* is a factor (*n* = 1 for minimum dislocation density).

Figure 5b shows the (110) diffraction plane of all the samples. There was a slight shift in the lower angle of 2θ as the concentration of NiO NPs increased to N-20, which might be due to a uniform tensile strain. With the further addition of NiO NPs (N-30 and N-40) into the perovskite precursor, there was a slight shift in the higher angle of 2θ. This could be due to the presence of compressive strain in the films, which could affect the crystallite size and crystallinity of the films.[31] Figure 5c and d show the dislocation density and microstrain of MAPbI3 N-10, N-20, N-30, and N-40. The estimated values are listed in Table I. As the concentration of NiO NPs was increased to N-20, the microstrain and

dislocation density of the perovskite films decreased, favoring the growth of crystallite size. The dislocation density is the reciprocal of crystallite size, and hence the N-20 perovskite film contains less dislocation than the pristine perovskite film. The other films showed increased microstrain and dislocation density values. Overall, the results indicate that the NiO NPs composite has a substantial impact on the growth and crystallization of perovskite films.[32]

UV and PL Spectral Analysis

The optical properties of perovskite films with and without NiO NP composite were studied. Figure 6a shows the UV–Vis absorption spectra of perovskite films. It is observed that the perovskite films with NiO composite have better absorbance when compared to the pristine perovskite films. This may be due to the better crystallinity and large grain size contained perovskite film, which is in good agreement with XRD and FESEM results.[33] The absorption of perovskite film was increased by increasing the concentration of NiO composite up to N-20. Further addition of NiO was suppressing the absorption property of the respective film.

To examine the potential photo-generated carrier extraction ability of perovskite film with different concentrations of NiO NPs, PL measurements were performed for perovskite films coated on glass slides. According to Fig. 6b, all perovskite films exhibited emission at 779 nm when they were excited at a wavelength of 517 nm, which is well in agreement with the UV-visible absorption spectrum. A strong emission peak was observed for the pristine perovskite film, while the films with NiO composite show quenched emission. The extraction of holes from the perovskite layer by the composited NiO indicates such quenched

Table I Values of the FWHM, crystallite size, strain and dislocation density

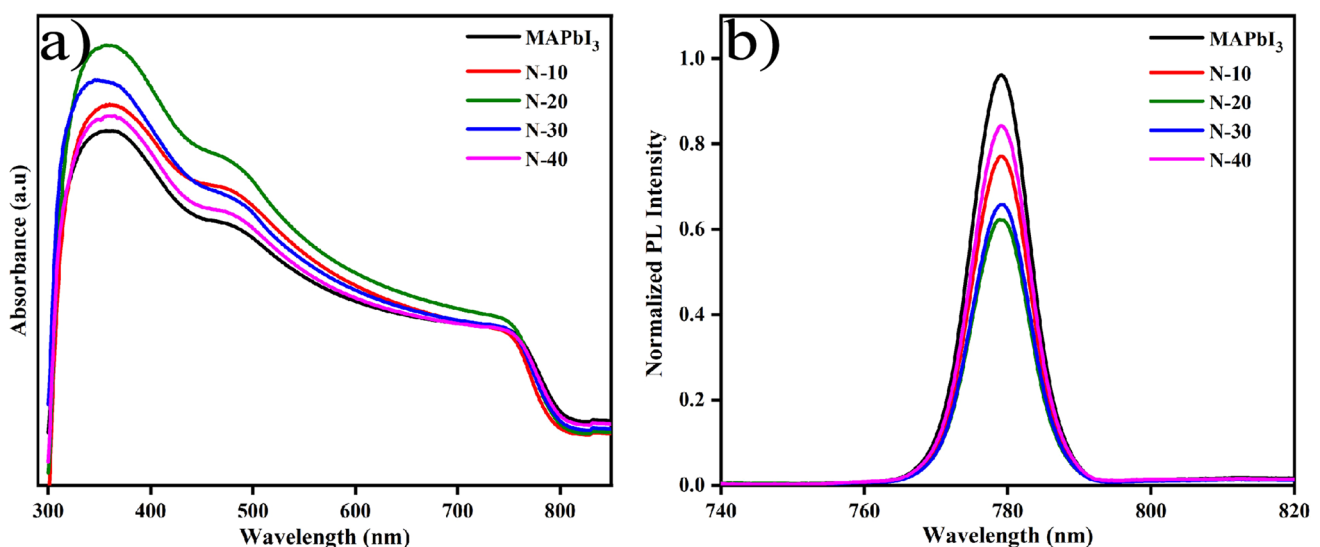| Sample	FWHM (°)	Crystallite size (nm)	Strain (10^{-5})	Dislocation density × 10^{14} (m^{-2})
MAPbI3	0.1052	76.11	5.6643	1.7259
N-10	0.0976	82.02	5.2571	1.4864
N-20	0.0922	86.77	4.9699	1.3282
N-30	0.0955	83.81	5.1433	1.4237
N-40	0.0964	83.01	5.1937	1.4513

Fig. 6 (a) and (b) The absorption spectra and the PL spectra of pristine MAPbI3, N-10, N-20, N-30, and N-40.

emission. It is worth noting that the perovskite film with N-20 showed the highest crystalline behavior with the largest grain size in XRD analysis, the highest light harvesting in UV-Vis spectrum analysis and efficient charge extraction behavior with PL quenching.

Figure 7 illustrates the schematic diagram of CPSC made of FTO/c-TiO$_2$/m-TiO$_2$/NiO/ MAPbI$_3$:NiO/carbon architecture with a band diagram. MAPbI$_3$ is a light-absorbing material and it has a band gap of 1.5 eV. The valence and conduction band levels are −5.4 eV and −3.9 eV, respectively. When light interacts with the MAPbI$_3$, electron–hole pairs are generated from the MAPbI$_3$. As the conduction band level of TiO$_2$ (−4.0 eV) matches the conduction band MAPbI$_3$, the generated electrons are transported to the FTO electrode via the electron transport layer, TiO$_2$. Similarly, as the valence band level of NiO (−5.3 eV) is closer to the level of valence band level MAPbI$_3$, the holes are transported to the carbon electrode via the hole transport layer, NiO. After introducing the mesoporous NiO spacer layer and composite NiO-MAPbI$_3$, the hole extraction process was further increased as NiO NPs closely interact with MAPbI$_3$ within the porous network. The result indicates that NiO:MAPbI$_3$ could have led to reduced charge recombination in the device.[34,35]

FESEM Image of Perovskite Films

FESEM was used to investigate the influence of NiO NPs on the morphology of the perovskite layer. Figure 8a–e shows

the surface view of prepared perovskite films without and with different weights of NiO NP composition. All the films exhibit randomly oriented heterogeneous crystallization with needle-shaped morphology. It is evident that the perovskite film without NiO NP composite exhibits large number of voids when compared to the films with NiO composite. For further detailed investigation, histogram of needle width distribution of perovskite grains in all films was plotted by measuring the width of 60 numbers of needle shaped morphology in each corresponding FESEM images. The plotted histogram of needle width distribution of pristine and NiO composited MAPbI$_3$ film is shown in Fig. 9a–e. The obtained average needle width of pristine MAPbI$_3$, N-10, N-20, N-30, and N-40 are 1.88 μm, 2.33 μm, 3.71 μm, 3.21 μm, and 2.33 μm, respectively. From this result, it is again confirmed that the needle width size of pristine perovskite film is smaller when compared to films with NiO composition. This lower width size with a large number of voids leads to the generation of more charge carrier recombination at the surface. On the other hand, NiO composition over N-20 suppresses the width size of perovskite. This reduced width size may be due to the occurrence of stress at the grain boundaries. As a result, they have more grain boundaries than perovskite film N- 20, which also affect the performance of the respective devices through increased non-radiative recombination.[36–38] Figure S1 (a–e) shows the EDS spectra of pristine and composite perovskite films. The weight percentage of each element in all perovskite films is shown in Table II. The presence of NiO NPs can
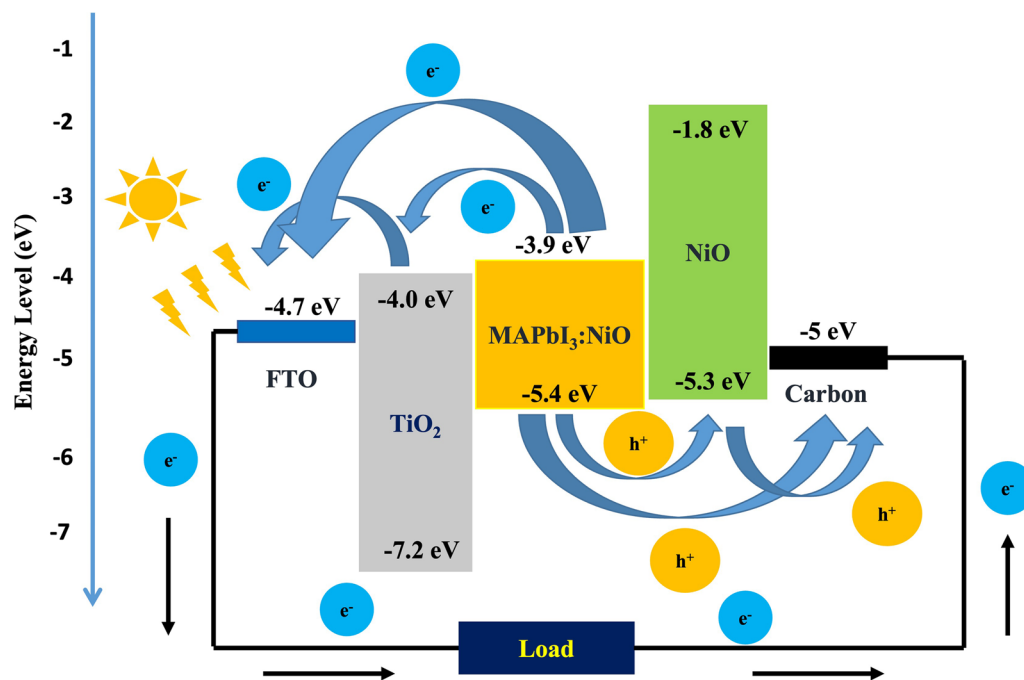

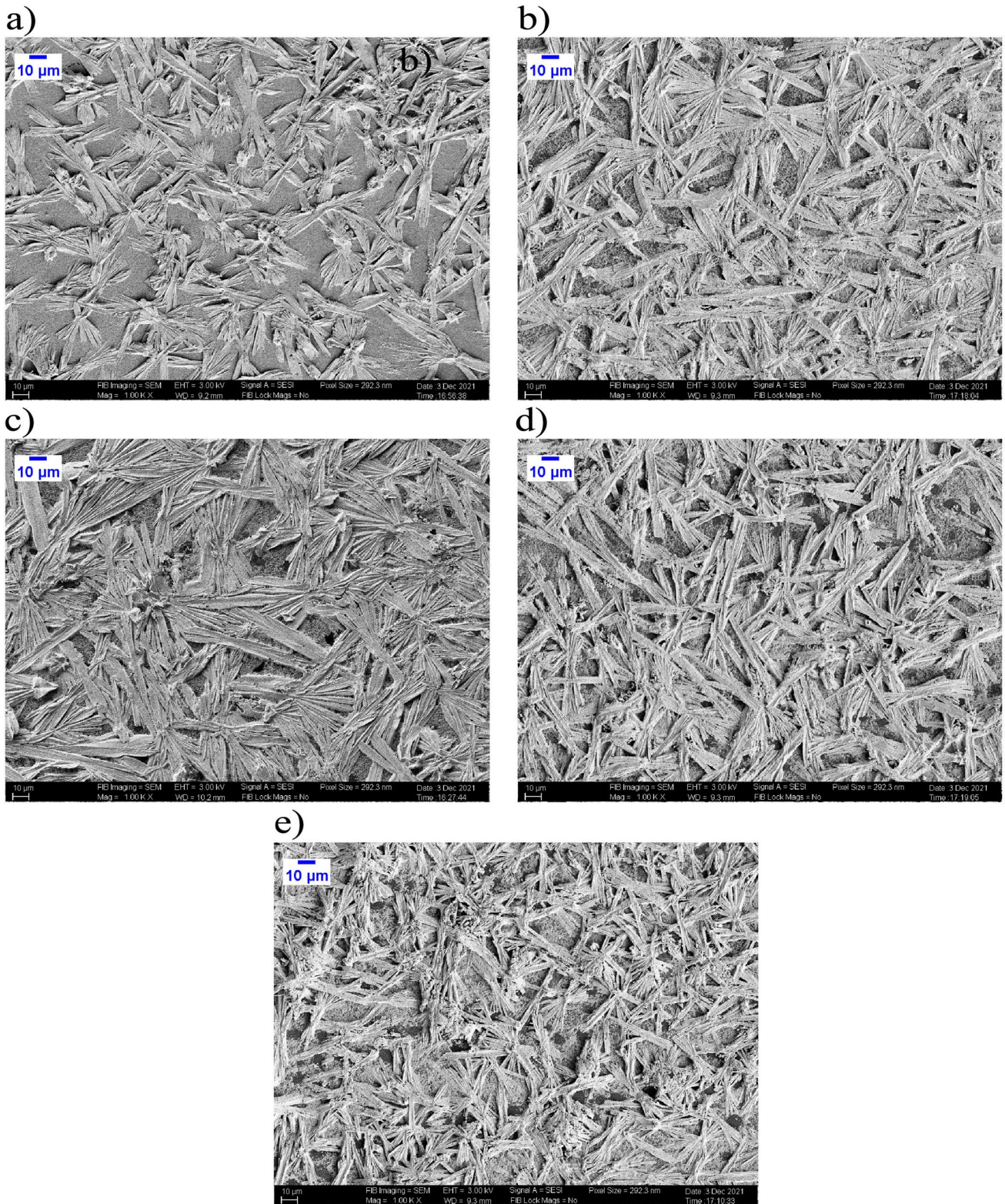**Fig. 7** Schematic band diagram and the charge transfer process of CPSC with NiO spacer layer.

a)

b)

c)

d)

e)

Fig. 8 (a–e) FESEM image of pristine MAPbI$_3$, N-10, N-20, N-30, and N-40.
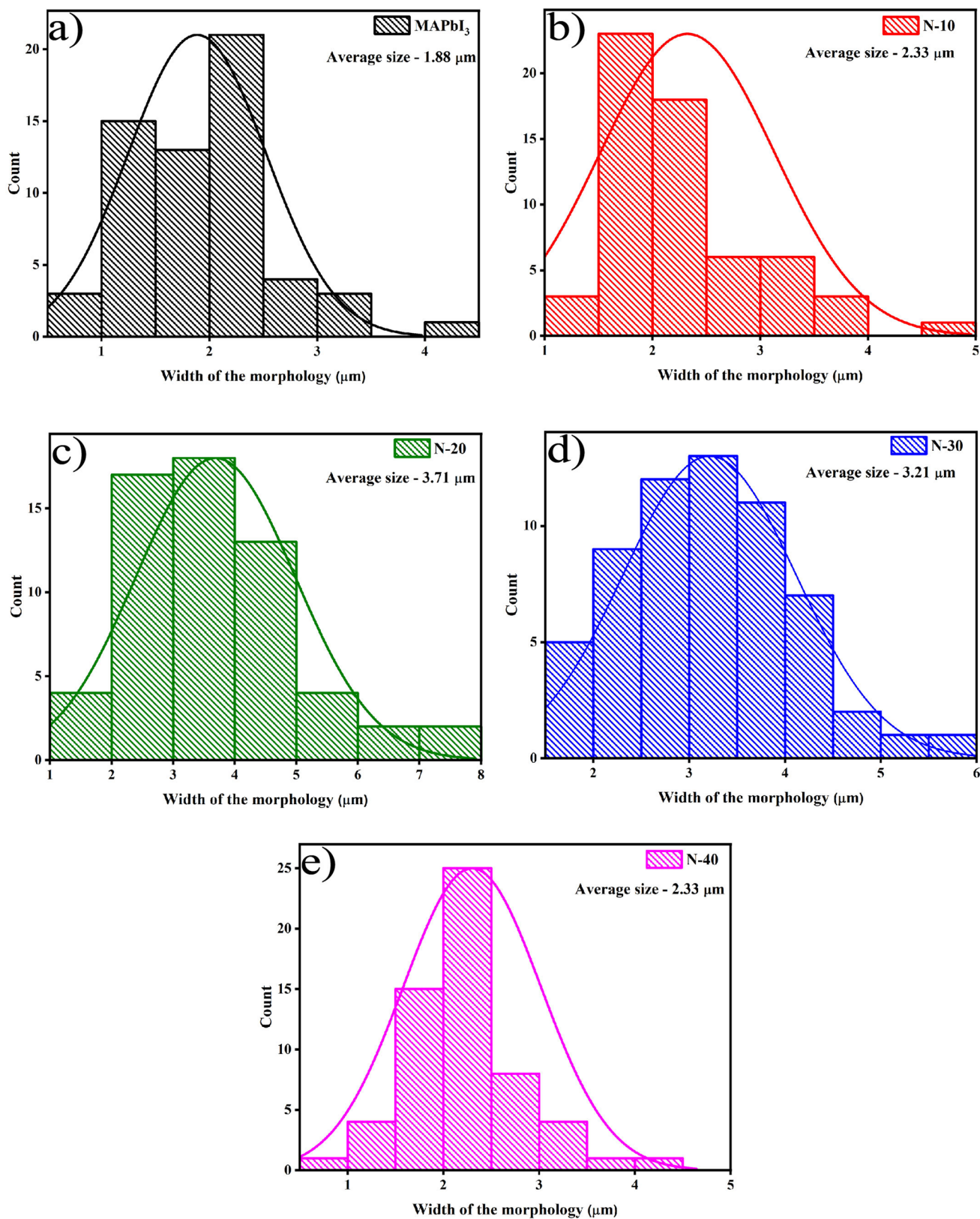
Fig. 9 (a–e) Histogram of needle width distribution of pristine MAPbI$_3$, N-10, N-20, N-30, and N-40.

Table II Weight% of each element in pristine MAPbI$_3$ and MAPbI$_3$:NiO NP composite films

Sample	C	N	O	Ti	Ni	I	Pb	Total
MAPbI$_3$	2.70	2.87	11.56	8.17	–	46.92	27.78	100
N-10	2.90	2.46	10.35	7.63	1.29	50.89	24.49	100
N-20	2.58	2.15	10.02	7.34	1.85	48.15	27.92	100
N-30	2.71	2.26	9.40	5.97	2.51	50.84	26.31	100
N-40	2.75	1.76	8.59	5.57	3.03	50.91	27.40	100

be identified in the same composite films; however, EDS is unable to detect the presence of hydrogen. Titanium element was found in all perovskite films because the perovskite layer was coated on the TiO$_2$ layer. In the pristine MAPbI$_3$ film, oxygen element was observed as a result of the pristine perovskite coated on the TiO$_2$. The uniform distribution of NiO NPs in the perovskite film is observed in the elemental analysis of N-20 film and it is shown in Fig. S2. In addition,

the elements such as carbon, nitrogen, oxygen, iodide, lead and nickel are distributed uniformly throughout the film.

Figure 10a shows a FESEM cross-sectional image of a solar cell made of FTO/c-TiO$_2$/m-TiO$_2$/NiO/MAPbI$_3$:NiO NP/carbon. The c-TiO$_2$, m-TiO$_2$, NiO, MAPbI$_3$-NiO, and carbon layers have thicknesses of 60 nm, 450 nm, 280 nm, 780 nm, and 20 μm, respectively. The photograph of the fabricated device is shown in Fig. 10b. The structural, thermal
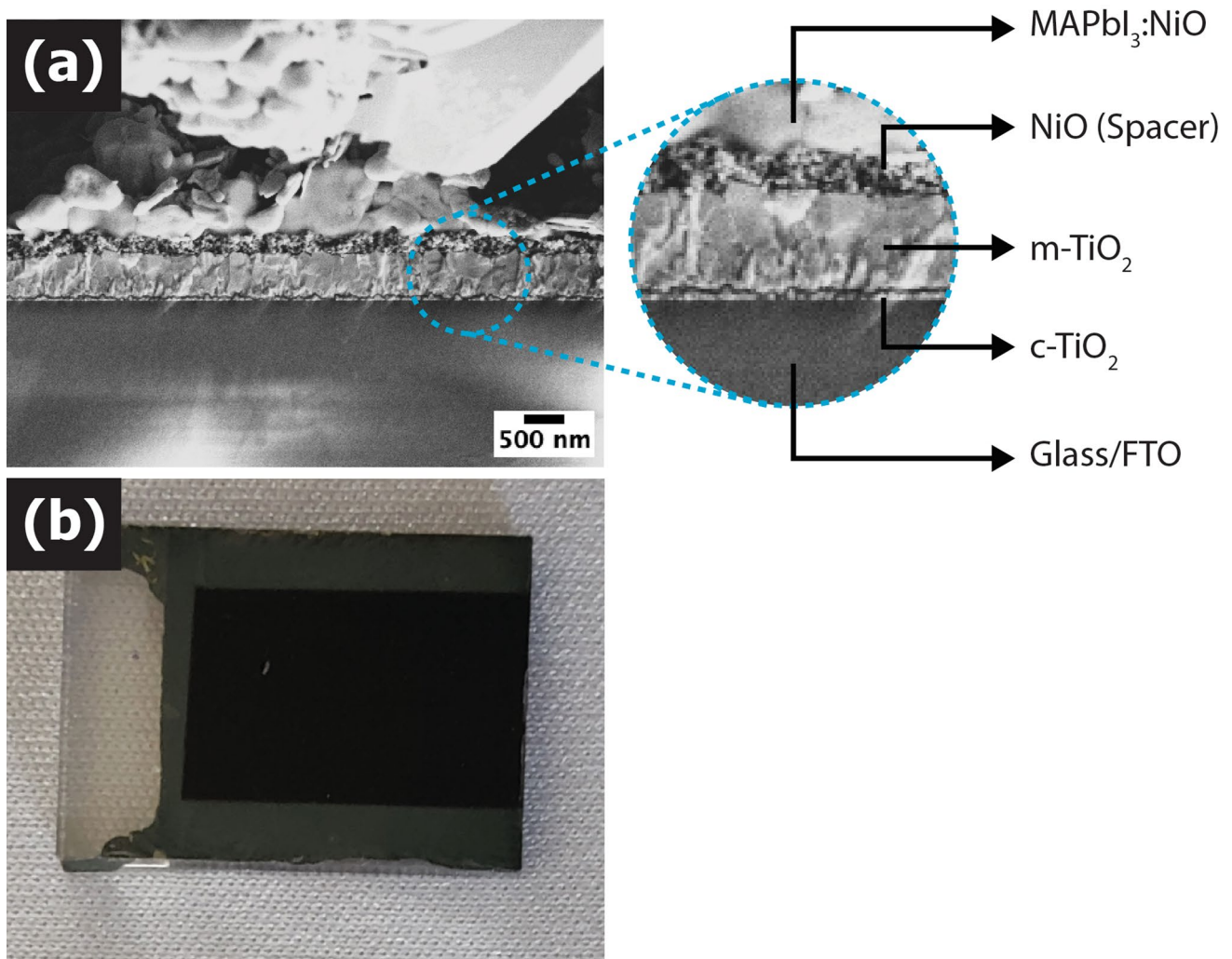

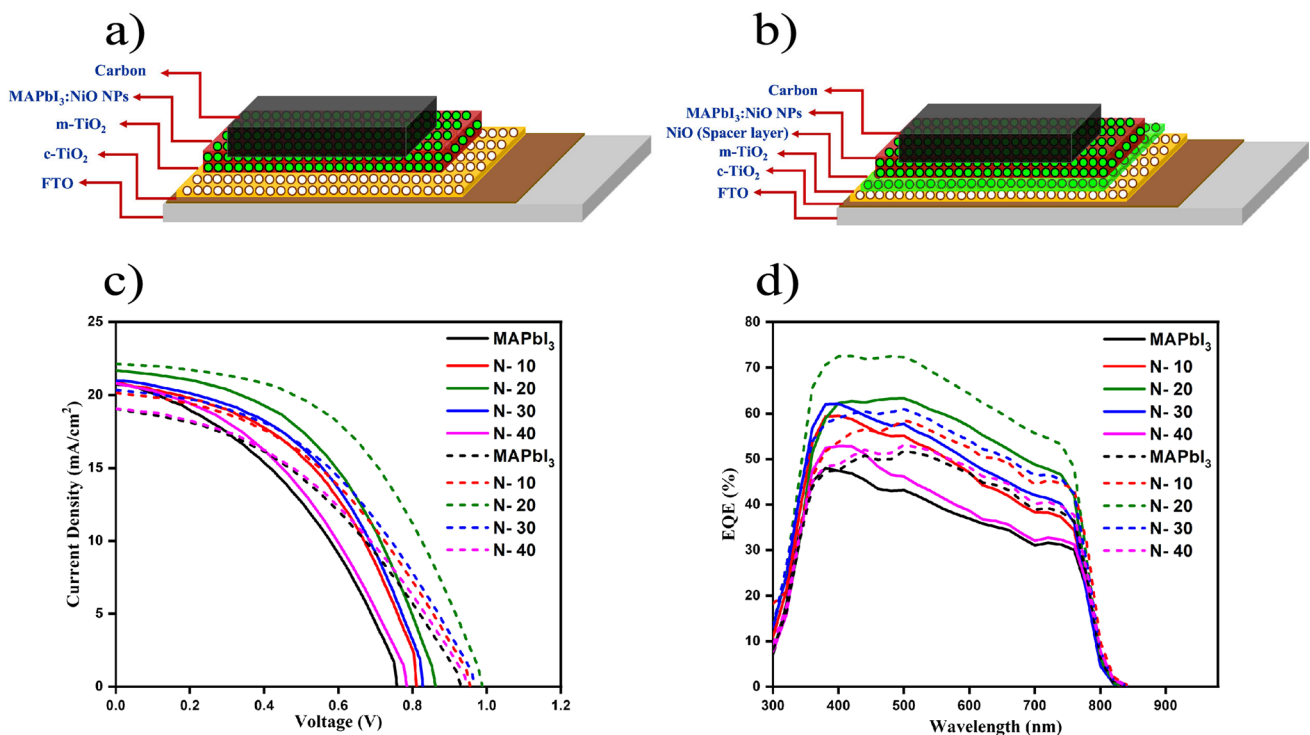**Fig. 10** (a) Cross-sectional FESEM image of N-20 device and (b) photograph of N-20 device.

Fig. 11 (a) and (b) Architecture of MAPbI$_3$:NiO NP composite-based CPSC without and with spacer layer configurations. (c) and (d) J–V characteristics and EQE spectra of MAPbI$_3$:NiO NP composite-based CPSC without (solid line) and with (dashed line) spacer layer configurations.

Table III J–V parameters of CPSC without spacer layer

Samples	J_{sc} (mA cm^{-2})	V_{oc} (mV)	Fill factor (FF)	η (%)
MAPbI$_3$	20.728	758	40.6	6.38
N-10	20.788	811	47.5	8.00
N-20	21.676	862	52.2	9.75
N-30	20.988	828	48.1	8.36
N-40	20.796	785	41.5	6.77

Table IV J–V parameters of MAPbI$_3$:NiO NP composite CPSC with NiO spacer layer

Samples	J_{sc} (mA cm^{-2})	V_{oc} (mV)	Fill factor (FF)	η (%)
MAPbI$_3$	19.076	949	41.3	7.48
N-10	20.152	955	43.1	8.29
N-20	22.112	988	50.2	10.97
N-30	20.364	969	43.8	8.64
N-40	19.048	930	41.2	7.30

and sheet resistance characteristics of the conductive carbon layer are given in Fig. S3.

J–V Characteristics and EQE Spectra of Fabricated CPSC without and with Spacer Layer

The performance of fabricated CPSC with the architecture of FTO/c-TiO$_2$/m-TiO$_2$/MAPbI$_3$:NiO/carbon and FTO/c-TiO$_2$/m-TiO$_2$/m-NiO/MAPbI$_3$:NiO/carbon are investigated by the J–V measurement and are shown in Fig. 11a and b. The obtained J–V curves of the devices are shown in Fig. 11c and the corresponding J–V parameters are listed in Tables III and IV. The pristine perovskite device shows PCE of 6.38% with a short-circuit current density (J_{sc}) of 20.728 mA/cm^2, an open-circuit voltage (V_{oc}) of 0.758 V, and a fill factor (FF) of 40.6%. Among all CPSCs, the solar cell made with N-20

achieved the highest PCE of 9.75% with a J_{sc} of 21.676 mA/cm^2, V_{oc} of 0.862 V and a FF of 52.2%. It was observed that the V_{oc} and FF of the device with N-20 was found to be increased well compared to other devices. Such enhanced V_{oc} and FF of the respective device might be due to reduced non-radiative recombination and crystal defects due to the passivation effect of the NiO composite, which enhances the carrier generation as well as the hole extraction.[39] Overall, the incorporation of N-20 into the perovskite precursor led to the formation of large grains of perovskite, which enhanced the performance of the PV device. From the performance of the device which has pristine perovskite layer with a spacer layer, it is evident that the additional spacer layer enhances the V_{oc} of the respective device (949 mV) when compared to the same architecture device without a

spacer layer (758 mV). The reduction of recombination at the perovskite/carbon may be the reason for this enhancement of V_{oc} and the corresponding device exhibits PCE of 7.48% with a J_{sc} of 19.076 mA/cm^2, and a FF of 41.3%. In the same way, the additional spacer layer enhances V_{oc} and PCE compared to the same devices fabricated without a spacer layer. The obtained V_{oc} of the device pristine MAPbI$_3$, N-10, N-20, N-30, and N-40 devices are 949 mV, 955 mV, 988 mV, 969 mV, and 930 mV, respectively. Here also the device with N-20 NiO composite perovskite layer with an additional spacer layer achieved the highest PCE of 10.97% with an improved voltage of 988 mV from 862 mV (N-20 without a spacer layer).

Figure 11d shows the EQE spectra of devices with and without the NiO composited perovskite layer. The EQE spectra show that the maximum photocurrent production occurs in the visible region for all devices. More importantly, devices without and with a spacer layer of N-20 have higher EQE with more than 60% and 70% in the visible range. It is evident that the CPSC based on the N-20 perovskite device generated a higher EQE than all other devices. This enhancement was due to the high absorbance and large grain size of the respective perovskite layer. Furthermore, the results of the EQE are closely matched with the UV-visible absorption spectra. The NiO NPs and NiO spacer layer of CPSC devices provide efficient paths for fast hole extraction to the electrode, resulting in the transport of more electrons in the perovskite layer from the mp-TiO$_2$ to c-TiO$_2$ layers, which leads to an increase in current density. The enhancement of EQE values with and without the spacer layer of the NiO composite-based CPSC device was attributed to effective charge extraction, higher light absorption and reduced charge recombination.

Conclusion

In summary, NiO NPs were synthesized by co-precipitation method with EDTA as a capping agent. The phase purity and crystallinity of the synthesized NiO NPs were confirmed by the PXRD pattern. The FESEM image confirmed the mixed spherical and oval shape of NiO NPs. Further, different weights of synthesized NiO NPs were incorporated into the perovskite layer, and the effect of incorporation of NiO NPs was analyzed in terms of the optical and morphological properties. The inclusion of p-type semiconductor material (NiO NPs) induces crystallinity of perovskite film with large grains and effectively passivates the perovskite grain boundaries, which results in reduced non-radiative recombination. The solar cell with N-20 NiO NPs composition in perovskite provides a maximum power conversion efficiency of 9.75%. Moreover, the effect of the addition of a NiO-based spacer layer in the same device configuration

was studied in detail. A champion device (N-20) with PCE of 10.97% was achieved with the help of a spacer layer by improving the V_{oc} from 862 mV to 988 mV. In addition to the spacer layer which improves the V_{oc}, the incorporation of NiO NPs controls the perovskite film formation, which leads to an increase in the light absorption and improves the charge separation and fast hole extraction in the film. The results show that the addition of NiO NPs in the perovskite precursor provides a way to boost the performance of the PV device.

References

1. K. Zheng, Q. Zhu, M. Abdellah, M.E. Messing, W. Zhang, A. Generalov, Y. Niu, L. Ribaud, S.E. Canton, and T. Pullerits, Exciton binding energy and the nature of emissive states in organometal halide perovskites. *J. Phys. Chem. Lett.* 6, 2969 (2015).

2. Z. Xiao, Y. Yuan, Q. Wang, Y. Shao, Y. Bai, Y. Deng, Q. Dong, M. Hu, C. Bi, and J. Huang, Thin-film semiconductor perspective of organometal trihalide perovskite materials for high-efficiency solar cells. *Mater. Sci. Eng. R Rep.* 101, 1 (2016).

3. H. Wei, Y. Fang, P. Mulligan, W. Chuirazzi, H.-H. Fang, C. Wang, B.R. Ecker, Y. Gao, M.A. Loi, and L. Cao, Sensitive x-ray detectors made of methylammonium lead tribromide perovskite single crystals. *Nat. Photonics* 10, 333 (2016).

4. M. Li, Z.-K. Wang, T. Kang, Y. Yang, X. Gao, C.-S. Hsu, Y. Li, and L.-S. Liao, Graphdiyne-modified cross-linkable fullerene as an efficient electron-transporting layer in organometal halide perovskite solar cells. *Nano Energy* 43, 47 (2018).

5. G. Sadoughi, D.E. Starr, E. Handick, S.D. Stranks, M. Gorgoi, R.G. Wilks, M. Bär, and H.J. Snaith, Observation and mediation of the presence of metallic lead in organic–inorganic perovskite films. *ACS Appl. Mater. Interfaces* 7, 13440 (2015).

6. W. Ke, G. Fang, Q. Liu, L. Xiong, P. Qin, H. Tao, J. Wang, H. Lei, B. Li, J. Wan, G. Yang, and Y. Yan, Low-temperature solution-processed tin oxide as an alternative electron transporting layer for efficient perovskite solar cells. *J. Am. Chem. Soc.* 137, 6730 (2015).

7. J. Cao, B. Wu, R. Chen, Y. Wu, Y. Hui, B.-W. Mao, and N. Zheng, Efficient, hysteresis-free, and stable perovskite solar cells with zno as electron-transport layer: effect of surface passivation, advanced materials. *Adv. Mater.* 30, 1705596 (2018).

8. J.H. Heo, H.J. Han, D. Kim, T.K. Ahn, and S.H. Im, Hysteresis-less inverted CH$_3$NH$_3$PbI$_3$ planar perovskite hybrid solar cells with 18.1% power conversion efficiency. *Energy Environ. Sci.* 8, 1602 (2015).

9. H. Chen, Y. Chen, T. Zhang, X. Liu, X. Wang, and Y. Zhao, Advances to high-performance black-phase FAPbI$_3$ perovskite

for efficient and stable photovoltaics. *Small Struct.* 2, 2000130 (2021).

10. J. Kim, N. Park, J.S. Yun, S. Huang, M.A. Green, and A.W.Y. Ho-Baillie, An effective method of predicting perovskite solar cell lifetime—case study on planar $CH_3NH_3PbI_3$ and $HC(NH_2)_2PbI_3$ perovskite solar cells and hole transfer materials of spiro-OMeTAD and PTAA. *Sol. Energy. Mater. Sol. Cells* 162, 41 (2017).

11. Y. Zhang, M. Elawad, Z. Yu, X. Jiang, J. Lai, and L. Sun, Enhanced performance of perovskite solar cells with P3HT hole-transporting materials via molecular p-type doping. *RSC Adv.* 6, 108888 (2016).

12. Z. Ku, Y. Rong, M. Xu, T. Liu, and H. Han, Full printable processed mesoscopic $CH_3NH_3PbI_3/TiO_2$ heterojunction solar cells with carbon counter electrode. *Sci. Rep.* 3, 3132 (2013).

13. S. Maniarasu, T.B. Korukonda, V. Manjunath, E. Ramasamy, M. Ramesh, and G. Veerappan, Recent advancement in metal cathode and hole-conductor-free perovskite solar cells for low-cost and high stability: a route towards commercialization. *Renew. Sustain. Energy Rev.* 82, 845 (2018).

14. P. Qin, S. Tanaka, S. Ito, N. Tetreault, K. Manabe, H. Nishino, M.K. Nazeeruddin, and M. Grätzel, Inorganic hole conductor-based lead halide perovskite solar cells with 12.4% conversion efficiency. *Nat. Commun.* 5, 3834 (2014).

15. A.S. Subbiah, A. Halder, S. Ghosh, N. Mahuli, G. Hodes, and S.K. Sarkar, Inorganic hole conducting layers for perovskite-based solar cells. *J. Phys. Chem. Lett.* 5, 1748 (2014).

16. J.A. Christians, R.C.M. Fung, and P.V. Kamat, An inorganic hole conductor for organo-lead halide perovskite solar cells. Improved hole conductivity with copper iodide. *J. Am. Chem. Soc.* 136, 758 (2014).

17. X. Xu, Z. Liu, Z. Zuo, M. Zhang, Z. Zhao, Y. Shen, H. Zhou, Q. Chen, Y. Yang, and M. Wang, Hole selective NiO contact for efficient perovskite solar cells with carbon electrode. *Nano Lett.* 15, 2402 (2015).

18. Z. Liu, M. Zhang, X. Xu, L. Bu, W. Zhang, W. Li, Z. Zhao, M. Wang, Y.-B. Cheng, and H. He, p-Type mesoscopic NiO as an active interfacial layer for carbon counter electrode based perovskite solar cells. *Dalton Trans.* 44, 3967 (2015).

19. J.-Y. Jeng, K.-C. Chen, T.-Y. Chiang, P.-Y. Lin, T.-D. Tsai, Y.-C. Chang, T.-F. Guo, P. Chen, T.-C. Wen, and Y.-J. Hsu, Nickel oxide electrode interlayer in $CH_3NH_3PbI_3$ perovskite/PCBM planar-heterojunction hybrid solar cells. *Adv. Mater.* 26, 4107 (2014).

20. L. Hu, J. Peng, W. Wang, Z. Xia, J. Yuan, J. Lu, X. Huang, W. Ma, H. Song, W. Chen, Y.-B. Cheng, and J. Tang, Sequential deposition of $CH_3NH_3PbI_3$ on planar NiO film for efficient planar perovskite solar cells. *ACS Photonics* 1, 547 (2014).

21. A.A. Jabbar, A.J. Haider, M.J. Haider, and K.F. Al-azawi, Preparation and characterization of NiO/PSi as self-cleaning surface. *J. Mater. Res. Technol.* 9, 15123–15131 (2020).

22. B. Mustafa, J. Griffin, A.S. Alsulami, D.G. Lidzey, and A.R. Buckley, Solution processed nickel oxide anodes for organic photovoltaic devices. *Appl. Phys. Lett.* 104, 063302 (2014).

23. F. Jiang, W.C.H. Choy, X. Li, D. Zhang, and J. Cheng, Post-treatment-free solution-processed non-stoichiometric NiOx nanoparticles for efficient hole-transport layers of organic optoelectronic devices. *Adv. Mater.* 27, 2930 (2015).

24. M.-H. Li, P.-S. Shen, K.-C. Wang, T.-F. Guo, and P. Chen, Inorganic p-type contact materials for perovskite-based solar cells. *J. Mater. Chem. A* 3, 9011 (2015).

25. J.H. Park, J. Seo, S. Park, S.S. Shin, Y.C. Kim, N.J. Jeon, H.-W. Shin, T.K. Ahn, J.H. Noh, S.C. Yoon, C.S. Hwang, and S.I. Seok, Efficient $CH_3NH_3PbI_3$ perovskite solar cells employing nanostructured p-type NiO electrode formed by a pulsed laser deposition. *Adv. Mater.* 27, 4013 (2015).

26. X. Zheng, Z. Song, Z. Chen, S.S. Bista, P. Gui, N. Shrestha, C. Chen, C. Li, X. Yin, R.A. Awni, H. Lei, C. Tao, R.J. Ellingson, Y. Yan, and G. Fang, Interface modification of sputtered NiOx as the hole-transporting layer for efficient inverted planar perovskite solar cells. *J. Mater. Chem. C* 8, 1972 (2020).

27. H.T. Rahal, R. Awad, A.M. Abdel-Gaber, and D. El-Said Bakeer, Synthesis, characterization, and magnetic properties of pure and EDTA-capped NiO nanosized particles. *J. Nanomater.* 2017, 9 (2017).

28. S. Khalid, M.A. Malik, D.J. Lewis, P. Kevin, E. Ahmed, Y. Khan, and P. O'Brien, Transition metal doped pyrite (FeS_2) thin films: structural properties and evaluation of optical band gap energies. *J. Mater. Chem. C* 3, 12068 (2015).

29. C.C. Stoumpos, C.D. Malliakas, and M.G. Kanatzidis, Semiconducting tin and lead iodide perovskites with organic cations: phase transitions, high mobilities, and near-infrared photoluminescent properties. *Inorg. Chem.* 52, 9019 (2013).

30. I. Robinson and R. Harder, Coherent X-ray diffraction imaging of strain at the nanoscale. *Nat. Mater.* 8, 291 (2009).

31. A.K. Zak, W.H.A. Majid, M.E. Abrishami, and R. Yousefi, X-ray analysis of ZnO nanoparticles by Williamson–Hall and size–strain plot methods. *Solid State Sci.* 13, 251 (2011).

32. J. Bahadur, A.H. Ghahremani, S. Gupta, T. Druffel, M.K. Sunkara, and K. Pal, Enhanced moisture stability of $MAPbI_3$ perovskite solar cells through barium doping. *Sol. Energy* 190, 396 (2019).

33. N. Besra, S. Pal, B.K. Das, and K.K. Chattopadhyay, Perovskites beyond photovoltaics: field emission from morphology-tailored nanostructured methylammonium lead triiodide. *Phys. Chem. Chem. Phys.* 19, 26708 (2017).

34. J.H. Heo, S.H. Im, J.H. Noh, T.N. Mandal, C.S. Lim, J.A. Chang, Y.H. Lee, H.J. Kim, A. Sarkar, M.K. Nazeeruddin, and M. Grätzel, Efficient inorganic–organic hybrid heterojunction solar cells containing perovskite compound and polymeric hole conductors. *Nat. Photonics* 7, 486 (2013).

35. D.S. Mann, P. Patil, D.H. Kim, S.N. Kwon, and S.I. Na, Boron nitride-incorporated NiOx as a hole transport material for high-performance pin planar perovskite solar cells. *J. Power Sources* 477, 228738 (2020).

36. Y. Yang, H. Peng, C. Liu, Z. Arain, Y. Ding, S. Ma, X. Liu, T. Hayat, A. Alsaedi, and S. Dai, Bi-functional additive engineering for high-performance perovskite solar cells with reduced trap density. *J. Mater. Chem. A* 7, 6450 (2019).

37. M. Yang, Y. Zeng, Z. Li, D.H. Kim, C.-S. Jiang, J. van de Lagemaat, and K. Zhu, Do grain boundaries dominate non-radiative recombination in $CH_3NH_3PbI_3$ perovskite thin films? *Phys. Chem. Chem. Phys.* 19, 5043 (2017).

38. D. Gedamu, I.M. Asuo, D. Benetti, M. Basti, I. Ka, S.G. Cloutier, F. Rosei, and R. Nechache, Solvent-antisolvent ambient processed large grain size perovskite thin films for high-performance solar cells. *Sci. Rep.* 8, 12885 (2018).

39. C.M. Wolff, P. Caprioglio, M. Stolterfoht, and D. Neher, Nonradiative recombination in perovskite solar cells: the role of interfaces. *Adv. Mater.* 31, 1902762 (2019).

Authors and Affiliations

R. Isaac Daniel[1] · R. Govindaraj[1] · P. Ramasamy[1] · A. K. Chauhan[2,3,4]

✉ R. Govindaraj
isrogovindaraj@gmail.com

1   Department of Physics, SSN Research Centre, Sri
    Sivasubramaniya Nadar College of Engineering,
    Kalavakkam, Tamil Nadu 603110, India

2   Technical Physics Division, Organic Devices Section,
    Bhabha Atomic Research Centre, Mumbai 400085, India

3   Homi Bhabha National Institute, Mumbai 400094, India

4   Physics Department, C. C. S. University, Meerut 250004,
    India